Available at WWW.MATHEMATICSWEB.ORG POWERED BY SCIENCE DIRECT®

ELSEVIER

Journal of Computational and Applied Mathematics 152 (2003) 199–216

JOURNAL OF COMPUTATIONAL AND APPLIED MATHEMATICS

www.elsevier.com/locate/cam

On the use of surface interpolation techniques in generalised finite volume strategies for simulating transport in highly anisotropic porous media

Pasdunkorale A. Jayantha*, Ian W. Turner

School of Mathematical Sciences, Gardens Point Campus, Queensland University of Technology, GPO Box 2434, Brisbane 4001, Australia

Received 26 November 2001; received in revised form 14 May 2002

Abstract

A control volume technique for solving a representative diffusion equation in an orthotropic medium is considered. The approximation of the cross-diffusion flux term is of utmost important for the accuracy of the solution. A preliminary investigation that used exact function values from an available analytical solution to approximate this term during the numerical simulation provided excellent agreement with the exact solution. This finding motivated the need for accurate surface interpolation techniques for estimating the cross-diffusion term. The use of radial basis functions is a well-known interpolation technique for fitting scattered data, which can be considered as a global interpolating method because function values in the whole solution domain contribute towards the interpolation. A number of radial basis functions (RBF) was used to approximate the gradients in the cross-diffusion flux term and it was found that the accuracy of the finite volume solution was generally poor. It was concluded that the RBF estimated function does not reflect local variation of the solution, particularly for the gradients. Another strategy for local function estimation concerns the weighted least-squares method. Different variants of this method were analysed here for approximating the cross-diffusion term and it was found that the numerical results well matched the exact solution. The results highlight that the development of an accurate, generalised finite volume strategy requires a highly accurate flux approximation to enable second-order spatial accuracy to be achieved.

Keywords: Discretized equations; Least squares; Overdetermined systems; Polynomial approximations

* Corresponding author.

E-mail addresses: jayanthapa@yahoo.com, pa.jayantha@fsc.qut.edu.au (P.A. Jayantha), i.turner@qut.edu.au (I.W. Turner).

0377-0427/03/$ - see front matter
PII: S0377-0427(02)00706-9

Nomenclature

A_k	length of a control volume face, m
C_p	specific heat, J kg^{-1} K^{-1}
F_k	midpoint of a control volume face
h	heat transfer coefficient, W m^{-2} K^{-1}
K	conductivity tensor, W m^{-1} K^{-1}
L	dimension of the domain in the x direction, m
M	dimension of the domain in the y direction, m
N	a representative node around a control volume
p	number of nodes around a control volume
$\hat{\mathbf{n}}$	unit outward normal vector at a CV face
P	node surrounded by a control volume
t	time, s
$\hat{\mathbf{t}}$	unit vector perpendicular to $\mathbf{v}$
$\hat{\mathbf{u}}$	unit vector along a control volume face
$\mathbf{v}$	vector through a CV face connecting adjacent nodes, m
$\mathbf{w}$	the vector representing $K^{\mathrm{T}}\hat{\mathbf{n}}$
x	coordinate length, m
y	coordinate length, m

Greek symbols

δt	discrete time step size, s
δV_P	area of a control volume, m^2
ρ	density, kg m^{-3}
ϕ	transported quantity, temperature, K
ϕ_0	initial temperature, K
ϕ_s	surrounding temperature, K

Superscripts and subscripts

k	index for the control volume faces
n	Represents nth time step

1. Introduction

The finite volume method has been widely employed for heat transfer, fluid flow and transport problems for more than two decades and has progressively been developed for solving nonlinear flow problems. This technique has been successfully applied for solving a range of different problems arising in various fields of science, technology and engineering [2,5,6,9,14,17,19,20,24,26]. Typically, due to the conservative characteristics of the scheme and its capability to be employed on either structured or unstructured meshes, it is the preferred method implemented in many industrial computational fluid dynamics codes.

The literature highlights only a limited number of computational schemes that model transport in highly anisotropic media on completely unstructured meshes using a generalised finite volume formulation [1,4,6,15,22]. The accuracy of the existing schemes is doubtful under extreme anisotropic ratios such as the one that exists in wood for permeability (of the order of 1:1000 in the radial versus longitudinal directions). This lacking of a reliable numerical method for such important industrial problems provides the motivation for this research.

Finite volume discretisation methods proceed by integrating the conservative law of interest across a discrete volume. This process generates a discrete analogue of the conservation law that balances the rate of change of mass, energy or momentum in the volume to the mass, energy or momentum fluxes gained or lost through the bounding surfaces of the volume. The second-order accuracy of the scheme, which will be described later in the text, depends to a large extent on the estimation of these flux terms at the midpoint of the control volume face [21]. For anisotropic problems this approximation is crucial and the classical linear models are often insufficient, especially when the anisotropy ratio is large and the flux vector is not always in the direction of the normal vector to the control volume face [12]. Note however, that this non-alignment of the direction of the flux and the normal vector at the control volume face is not a particularly of anisotropic media.

Usually the flux term is in the form $(K\nabla\phi)\cdot\hat{\mathbf{n}}$ where

$$K = \begin{pmatrix} k_{xx} & k_{xy} \\ k_{yx} & k_{yy} \end{pmatrix},$$

ϕ is the dependent function and $\hat{\mathbf{n}}$ is the outward unit normal vector at the finite volume surface. The approximation of this flux term can be rewritten for computational purposes in the form $\nabla\phi\cdot(K^{\mathrm{T}}\hat{\mathbf{n}})$. One can use function values at selected points of the solution domain to approximate the gradient. In the literature linear shape functions (hybrid techniques) are widely used to approximate these gradients [7,8,11,19], which leads to a fully implicit, first order in space, finite volume discretisation.

Alternatively the flux term can be decomposed into two terms as described below [4,12]. Consider the vector decomposition

$$\mathbf{w} = (K^{\mathrm{T}}\hat{\mathbf{n}}) = \alpha\mathbf{v} + \beta\hat{\mathbf{u}}, \tag{1}$$

where the scalars α and β involve K, the vector $\mathbf{v}$ and the unit vectors $\hat{\mathbf{n}}$ and $\hat{\mathbf{u}}$, see Figs. 1(c)–(d). One can show using vector algebra that

$$\alpha = \frac{\mathbf{w}\cdot\hat{\mathbf{n}}}{\mathbf{v}\cdot\hat{\mathbf{n}}} \quad \text{and} \quad \beta = \mathbf{w}\cdot\hat{\mathbf{u}} - \mathbf{w}\cdot\hat{\mathbf{n}}\,\frac{\mathbf{v}\cdot\hat{\mathbf{u}}}{\mathbf{v}\cdot\hat{\mathbf{n}}}.$$

The scalar product of Eq. (1) with $\nabla\phi$ yields

$$\nabla\phi\cdot(K^{\mathrm{T}}\hat{\mathbf{n}}) = \alpha\nabla\phi\cdot\mathbf{v} + \beta\nabla\phi\cdot\hat{\mathbf{u}},$$

which can be approximated at a control volume face (see Fig. 1(d)) as

$$\nabla\phi(\mathbf{x}_F)\cdot(K^{\mathrm{T}}\hat{\mathbf{n}}) \simeq \alpha(\phi_N - \phi_P) + \beta\nabla\phi(\mathbf{x}_F)\cdot\hat{\mathbf{u}}, \tag{2}$$

where $\nabla\phi(\mathbf{x}_F)$ represents the gradient of the function ϕ evaluated at the point F at the control volume face.

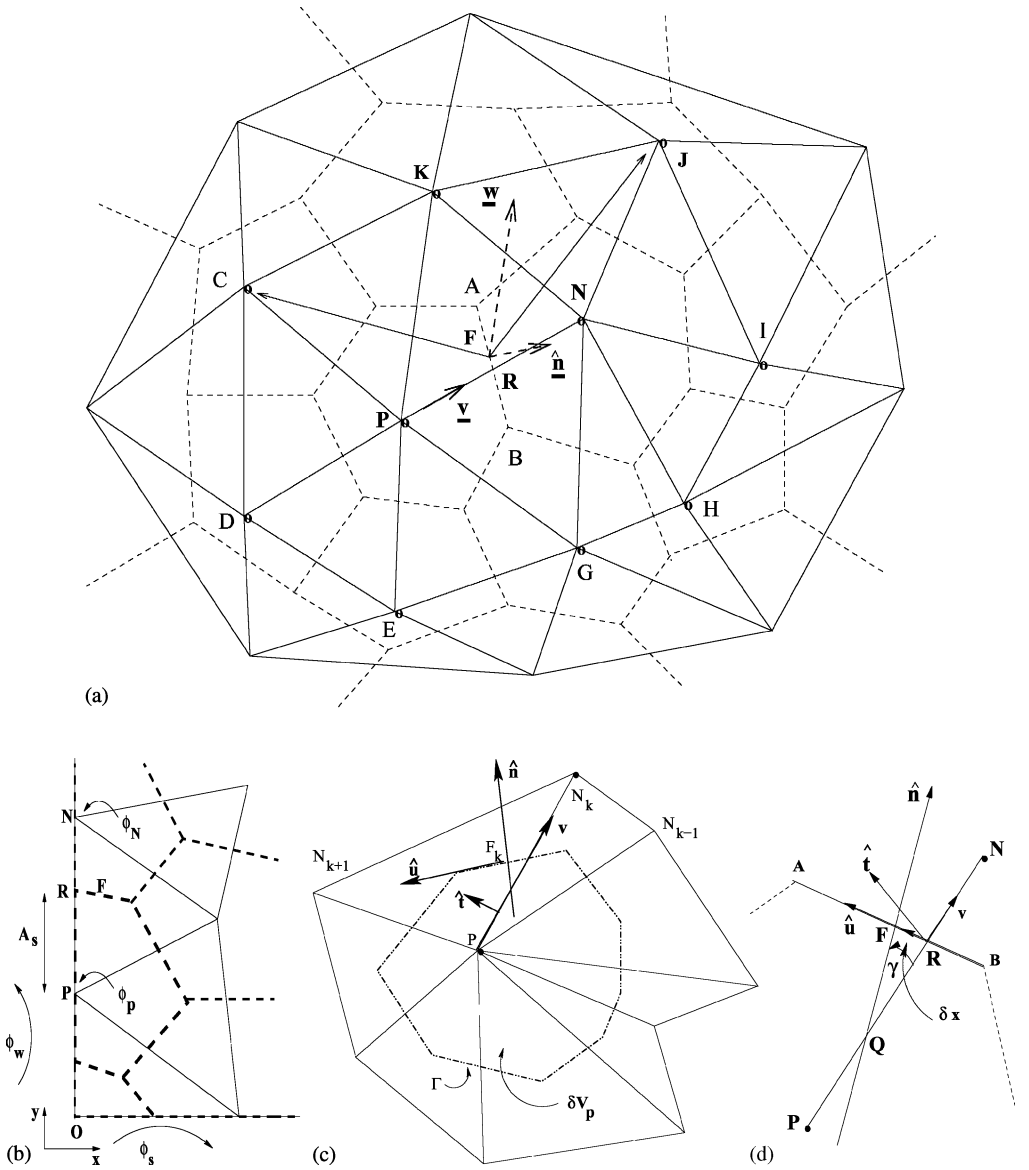

Fig. 1. (a) An example of a cluster of points used for the least-square approximation methods, (b) a boundary control volume, (c) a typical control volume and (d) a control volume face.

Note that the first term $(\phi_N - \phi_P)$ is a first-order approximation for the primary term $\nabla\phi(\mathbf{x}_F)\cdot\mathbf{v}$ and this will effect the accuracy of the finite volume scheme. The secondary flux term $\beta\nabla\phi\cdot\hat{\mathbf{u}}$ can be evaluated if the gradient at the control volume face is known. This paper discusses different techniques, based on radial basis functions [13,25], least-squares gradient reconstruction [3,10,11] and a function approximation technique using a weighted least-squares system of polynomial equations,

to approximate this term. The results were compared with the exact solution and also with the results obtained by using the linear shape functions.

In this work the following two-dimensional unsteady orthotropic diffusion equation for a finite rectangular domain is considered:

$$\rho C_p \frac{\partial \phi}{\partial t} = k_{xx} \frac{\partial^2 \phi}{\partial x^2} + k_{yy} \frac{\partial^2 \phi}{\partial y^2}, \quad 0 \leqslant x \leqslant L, \ 0 \leqslant y \leqslant M, \ t > 0, \tag{3}$$

where k_{xx} is very large (or small) when compared to k_{yy}. The boundary conditions and initial condition are defined as follows:

$$k_{xx} \frac{\partial \phi}{\partial x} = h(\phi - \phi_s) \text{ at } x = 0, \quad k_{xx} \frac{\partial \phi}{\partial x} = -h(\phi - \phi_s) \text{ at } x = L,$$

$$k_{yy} \frac{\partial \phi}{\partial y} = h(\phi - \phi_s) \text{ at } y = 0, \quad k_{yy} \frac{\partial \phi}{\partial y} = -h(\phi - \phi_s) \text{ at } y = M.$$

$$\phi(x, y, 0) = \phi_0 \text{ for } 0 \leqslant x \leqslant L, \ 0 \leqslant y \leqslant M$$

Such a system admits an analytical solution that can be exploited to assess the accuracy of the flux approximation methods under investigation.

2. Finite volume discretisation

The following finite volume discretisation technique for treating a generalised transport equation can be found in the literature [6,15,18,19,21]. The discretised form of the differential Eq. (3) is derived by integrating the equation over the control volume δV_p, see Fig. 1(c). The use of the Divergence theorem in the plane leads to

$$\rho C_p \frac{\mathrm{d}\bar{\phi}}{\mathrm{d}t} - \frac{1}{\delta V_P} \oint_{\Gamma} (K \nabla \phi) \cdot \hat{\mathbf{n}} \, \mathrm{d}\Gamma \simeq 0, \tag{4}$$

where

$$\bar{\phi} = \frac{1}{\delta V_P} \int_{\delta V_P} \phi \, \mathrm{d}V \tag{5}$$

is the average of ϕ in a control volume and Γ represents the boundary of the control volume. As there is no approximation made to this point, the Eq. (4) together with (5) is exact. Discretising Eq. (4) one can obtain

$$\rho C_p \frac{\mathrm{d}\bar{\phi}}{\mathrm{d}t} - \sum_{k=1}^{Np} \{(K \nabla \phi) \cdot \hat{\mathbf{n}}\}_{F_k} A_k \simeq 0, \tag{6}$$

which is second order in space if the term $(K \nabla \phi) \cdot \hat{\mathbf{n}}$ is accurately evaluated at the midpoint of the control volume face.

Assuming that ϕ_P represents the averaged value of ϕ over δV_P and considering the time integral from $n\delta t$ to $(n+1)\delta t$ the discrete form of Eq. (6) can be written as

$$\rho C_p \delta V_P(\phi_P^{(n+1)} - \phi_P^{(n)}) - \delta t \int_\Gamma (K\nabla\phi)^{(m)} \cdot \hat{\mathbf{n}}\, \mathrm{d}\Gamma \simeq 0,$$

where $n \leqslant m \leqslant n+1$. Approximating the integral as a summation using the midpoint rule and taking $m = n+1$, the above equation can be rewritten as

$$\rho C_p \delta V_P(\phi_P^{(n+1)} - \phi_P^{(n)}) - \delta t \sum_{k=1}^{p} (K\nabla\phi)_{F_k}^{(n+1)} \cdot \hat{\mathbf{n}}_\mathbf{k} A_k \simeq 0. \tag{7}$$

It is suggested here to replace the term $(K\nabla\phi)\cdot\hat{\mathbf{n}}_\mathbf{k}$ by Eq. (2) to obtain

$$\rho C_p \delta V_P(\phi_P^{(n+1)} - \phi_P^{(n)}) - \delta t \sum_{k=1}^{p} \overbrace{\alpha(\phi_{N_k}^{(n+1)} - \phi_P^{(n+1)})A_k}^{\text{Primary}}$$

$$- \delta t \sum_{k=1}^{p} \overbrace{\beta(\nabla\phi)_{F_k}^{(n+1)} \cdot \hat{\mathbf{u}}_\mathbf{k} A_k}^{\text{Secondary}} \simeq 0. \tag{8}$$

To approximate $(\nabla\phi)_{F_k}^{(n+1)} \cdot \hat{\mathbf{u}}_\mathbf{k}$ the following surface interpolation techniques were implemented and analysed to determine the accuracy of each method.

2.1. Radial basis functions (RBF)

Since there is no information concerning the function at time step $n+1$, one can approximate the secondary flux term as

$$(\nabla\phi)_{F_k}^{(n+1)} \cdot \hat{\mathbf{u}}_\mathbf{k} \simeq \frac{1}{A_k}(\phi_A^{(n)} - \phi_B^{(n)}), \tag{9}$$

where A and B are left and right states of the control volume face, respectively, see Fig. 1(d). This is itself a linear approximation and $\phi_A^{(n)}$ and $\phi_B^{(n)}$ must be found using interpolation methods involving the function values at the nth time step. It was found that this approximation gives good results if the exact function values taken from the derived analytical solution were used for $\phi_A^{(n)}$ and $\phi_B^{(n)}$. This result motivated the use of radial basis functions (RBF) using the known function values of the solution domain to approximate the required values as described in [13,25]. RBF schemes have provided excellent results for global function interpolation in the past.

It is assumed that the function ϕ may be written as a linear combination of M continuously differentiable basis functions, ψ

$$\phi(\mathbf{x}) = \sum_{j=1}^{M} a_j \psi_j(\mathbf{x} - \mathbf{x}_j), \tag{10}$$

where

$$\psi_j(\mathbf{x} - \mathbf{x}_j) = [(x - x_j)^2 + (y - y_j)^2 + c^2]^{1/2}$$

and c^2 is a nonzero input parameter. The unknown coefficients, a_j, are found by collocation

$$\phi(\mathbf{x}_i) = \sum_{j=1}^{M} a_j \psi_j(\mathbf{x}_i - \mathbf{x}_j),$$

using a set of node points $(x_i, y_i)_{i=1}^{M}$ over the solution domain, which forms a system of M linear equations in M unknowns of the form $\Lambda \underline{a} = \underline{\phi}$ where Λ is called the Grammian matrix. Once the coefficients, a_j, are found one can use Eq. (10) to estimate the function values for use in Eq. (9) at each control volume face. In this case Eq. (8) becomes

$$\rho C_p \delta V_P (\phi_P^{(n+1)} - \phi_P^{(n)}) - \delta t \sum_{k=1}^{p} \alpha (\phi_{N_k}^{(n+1)} - \phi_P^{(n+1)}) A_k \simeq \delta t \sum_{k=1}^{p} \beta (\phi_A^{(n)} - \phi_B^{(n)}). \tag{11}$$

2.2. Least-squares gradient reconstruction (LSGR)

Writing $(\nabla\phi)_P \cdot \mathbf{v}_k = (\partial\phi/\partial x_P \underline{\mathbf{i}} + \partial\phi/\partial y_P \underline{\mathbf{j}}) \cdot (\Delta x_k \underline{\mathbf{i}} + \Delta y_k \underline{\mathbf{j}}) \simeq \phi_{N_k} - \phi_P$ for each node connected to node P, N_k, $k = 1 \ldots p$, see Fig. 1(c), the following over-determined matrix system is obtained (see [3,10,11]).

$$\begin{pmatrix} \Delta x_1 & \Delta y_1 \\ \Delta x_2 & \Delta y_2 \\ \cdots & \cdots \\ \cdots & \cdots \\ \Delta x_p & \Delta y_p \end{pmatrix} \begin{pmatrix} \dfrac{\partial\phi}{\partial x}_P \\ \dfrac{\partial\phi}{\partial y}_P \end{pmatrix} = \begin{pmatrix} \phi_{N_1} - \phi_P \\ \phi_{N_2} - \phi_P \\ \cdots \\ \cdots \\ \phi_{N_p} - \phi_P \end{pmatrix}$$

or $B_{p\times 2}\Phi'_{2\times 1} = \mathbf{d}_{p\times 1}$. The gradient components that minimise $\|B\Phi' - \mathbf{d}\|^2$ in the least-squares sense with respect to a weighted inner product on $\mathbb{R}^p$ can be determined by multiplying the above system by $W_{p\times p} = \mathrm{Diag}(w_k)$ and B^{T}, to arrive at the normal equations $(B^{\mathrm{T}}WB)_{2\times 2}\Phi'_{2\times 1} = (B^{\mathrm{T}}W\mathbf{d})_{2\times 1}$. This system has the form

$$\begin{pmatrix} \displaystyle\sum_{k=1}^{p} w_k \Delta x_k^2 & \displaystyle\sum_{k=1}^{p} w_k \Delta x_k \Delta y_k \\ \displaystyle\sum_{k=1}^{p} w_k \Delta x_k \Delta y_k & \displaystyle\sum_{k=1}^{p} w_k \Delta y_k^2 \end{pmatrix} \begin{pmatrix} \dfrac{\partial\phi}{\partial x}_P \\ \dfrac{\partial\phi}{\partial y}_P \end{pmatrix} = \begin{pmatrix} \displaystyle\sum_{k=1}^{p} w_k \Delta x_k (\phi_{N_k} - \phi_P) \\ \displaystyle\sum_{k=1}^{p} w_k \Delta y_k (\phi_{N_k} - \phi_P) \end{pmatrix}. \tag{12}$$

Note that the weight coefficients, w_k's, are chosen so that more importance is given to the directions that are the closest neighbours of the point P as opposed to the nodes further away from the point P, see [3,10,11].

Once the gradients of the function are evaluated at each node of the mesh using a least-squares gradient reconstruction technique, it is possible to write

$$(\nabla\phi)_{F_k}^{(n+1)} \simeq \gamma(\nabla\phi)_P^{(n)} + (1-\gamma)(\nabla\phi)_{N_k}^{(n)},$$

where $PN_k : R_kN_k = 1 : \gamma$ and R_k is the intersection of line segments AB and PN_k, see Fig. 1(d). This expression was used for estimating the secondary flux term in Eq. (8) and hence it follows that

$$\rho C_p \delta V_P(\phi_P^{(n+1)} - \phi_P^{(n)}) - \delta t \sum_{k=1}^{p} \alpha(\phi_{N_k}^{(n+1)} - \phi_P^{(n+1)})A_k$$

$$\simeq \delta t \sum_{k=1}^{p} \beta[\gamma(\nabla\phi)_P^{(n)} + (1-\gamma)(\nabla\phi)_{N_k}^{(n)}] \cdot \hat{\mathbf{u}}_\mathbf{k} A_k. \tag{13}$$

2.3. Least-squares polynomial reconstruction (LSPR)

Consider the quadratic polynomial function approximation in the form

$$\phi(x, y) = a_1 + a_2 x + a_3 y + a_4 x^2 + a_5 xy + a_6 y^2. \tag{14}$$

Writing Eq. (14) for the r closest node points connected to the control volume face, for example, the nodes $C, D, E, G, H, I, J, K, N$ and P in Fig. 1(a), the following over-determined system of equations, $A\mathbf{X} = \mathbf{B}$, can be obtained.

$$\begin{pmatrix} 1 & x_1 & y_1 & .. & x_1y_1 & y_1^2 \\ 1 & x_2 & y_2 & .. & x_2y_2 & y_2^2 \\ .. & .. & & .. & .. & .. \\ .. & .. & & .. & .. & .. \\ .. & .. & & .. & .. & .. \\ 1 & x_r & y_r & .. & x_ry_r & y_r^2 \end{pmatrix} \begin{pmatrix} a_1 \\ a_2 \\ a_3 \\ .. \\ .. \\ a_6 \end{pmatrix} = \begin{pmatrix} \phi_1 \\ \phi_2 \\ \phi_3 \\ .. \\ .. \\ .. \\ \phi_r \end{pmatrix} \tag{15}$$

It was found that the use of six neighbouring points provided an ill-conditioned system matrix and consequently ten node points (or more, for distorted mesh) were used to generate the system. An equation related to the boundary conditions was added to the above system, for boundary control faces, see Fig. 1(b). For example, for the face F shown in Fig. 1(b), the equation,

$$\frac{\partial\phi}{\partial x} = \frac{h}{k_{xx}}(\phi - \phi_s), \text{ or } \frac{h}{k_{xx}}(\phi - \phi_s) = a_2 + 2a_4x + a_5y,$$

was also inserted into the system of equations given by Eq. (15).

The components that minimise $\|A\mathbf{X} - \mathbf{B}\|^2$ in the least-squares sense with respect to a weighted inner product on $\mathbb{R}^r$ can be determined by multiplying the above system by $W_{r\times r} = \mathrm{Diag}(w_k)$ and A^T, to arrive at the normal equations

$$(A^T W A)\mathbf{X} = (A^T W \mathbf{B}). \tag{16}$$

Again, as discussed in Section 2.2 the weight coefficients, w_k's, were chosen so that more importance is given to the nodes that are the closest neighbours of the point F. Solving the above system, it is

possible to find the function value and derivatives accurately at the point F on the control volume face and therefore the term $\nabla\phi\cdot\hat{\mathbf{u}}$ required for Eq. (8) can be estimated.

This method also was trailed to estimate the left and right states needed for use in Eq. (9), however, it was found that the direct use of the approximated gradients $\nabla\phi=(a_2+2a_4x+a_5y, a_3+a_5x+2a_6y)$ always gave superior results.

2.4. Linear shape functions (LSF)

This technique assumes that the function can be written as $\phi(x,y)=Ax+By+C$ where A,B, and C are constants for each triangular element. Further details of this technique can be found in [8,11,19]. In this case $\nabla\phi\cdot(K^{\mathrm{T}}\hat{\mathbf{n}}_k)^{(n+1)}$ is approximated directly and therefore Eq. (7) provides a fully implicit scheme in the form

$$\rho C_p\delta V_P(\phi_P^{(n+1)}-\phi_P^{(n)})-\alpha\delta t\sum_{k=1}^{p}\{(\hat{\mathbf{n}}_k^{(a)})^{\mathrm{T}}G_k^{(a)}(\mathbf{d}\phi_k^{(a)})^{(n+1)}A_k^{(a)}$$

$$+(\hat{\mathbf{n}}_k^{(b)})^{\mathrm{T}}G_k^{(b)}(\mathbf{d}\phi_k^{(b)})^{(n+1)}A_k^{(b)}\}\simeq 0, \tag{17}$$

where $G,\mathbf{d}\phi$ and $\hat{\mathbf{n}}_k$ are as described in [11,19].

2.5. Discretised equations

Each discretisation procedure discussed here produces an equation at each node point P in the following form:

$$\alpha_P\phi_P^{(n+1)}-\sum_{k=1}^{p}\beta_k\phi_{N_k}^{(n+1)}=\gamma_P\phi_P^{(n)}+\eta_P.$$

When all the nodes in a mesh have been visited a sparse linear system is formed and the resulting linear system is solved using a preconditioned *BiCGSTAB* method [23]. Numerical simulation codes, written in C++, were developed to obtain the solutions of the above linear systems.

3. Numerical results and discussion

The meshes shown in Fig. 2 were used to analyse the performance (in terms of efficiency and accuracy) of the flux approximation techniques proposed in Section 2. These meshes were created using EasyMesh [16] but the centres of the triangles were used to construct the control volumes in all cases tested. The benchmark transport problem given by Eq. (3) was considered for a material with the physical properties shown in Table 1.

For all cases, $\rho=600\ \mathrm{kg\ m^{-3}}$ and $C_p=1.6886\times10^3\ \mathrm{J\ kg^{-1}\ K^{-1}}$ were used with $\phi_0=30^{\circ}\mathrm{C}$ and $\phi_s=140^{\circ}\mathrm{C}$. Note that for mesh (i) and (ii) where the material has the dimensions $L=0.02$ m, $M=0.5$ m the boundaries at $x=0.02$ and $y=0.5$ were treated as symmetric planes where the fluxes were taken as zero; $(\partial\phi/\partial x)_L=0$ and $(\partial\phi/\partial y)_M=0$. For mesh (iii) where the material has dimensions $L=0.1$ m, and $M=0.04$ m, mixed boundary conditions were used for each boundary as stated in Section 1.

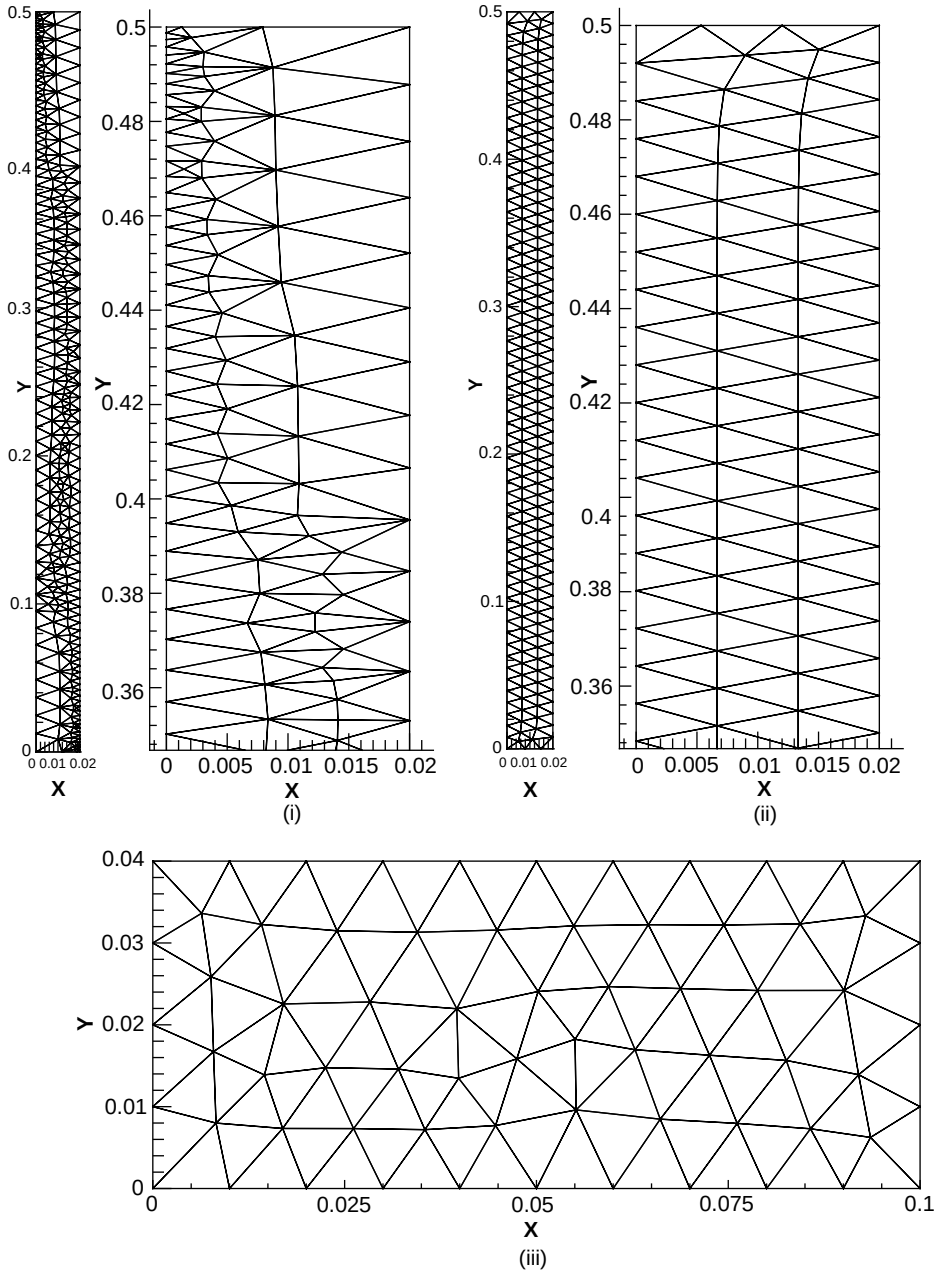

Fig. 2. Computational meshes used for all simulations (i) a distorted mesh; 0.02×0.5 m^2 (ii) an unstructured mesh; 0.02×0.5 m^2 and (iii) a coarse mesh; 0.1×0.04 m^2.

The results shown in Figs. 3–6 were obtained after 1000 s using the time step, $\delta t = 1$ s. It should be noted that the slight anomalies that appear in the computed solutions for all methods, including the exact solution, in Figs. 4(a) and 5(a) for distorted mesh (i) are due to the interpolation technique used in the plotting software and not artefacts of the numerical techniques.

Table 1
Physical parameters used for each case study

Case	h (W m^{-2} K^{-1})	k_{xx} (W m^{-1} K^{-1})	k_{yy} (W m^{-1} K^{-1})	L (m)	M (m)
1	10	0.154	1.54	0.02	0.5
2	10	0.154	154	0.02	0.5
3	30	0.154	1.54	0.02	0.5
4	30	0.154	154	0.02	0.5
5	10	0.154	154	0.1	0.04
6	10	154	0.154	0.1	0.04
7	10	1.2	1.2	0.1	0.04

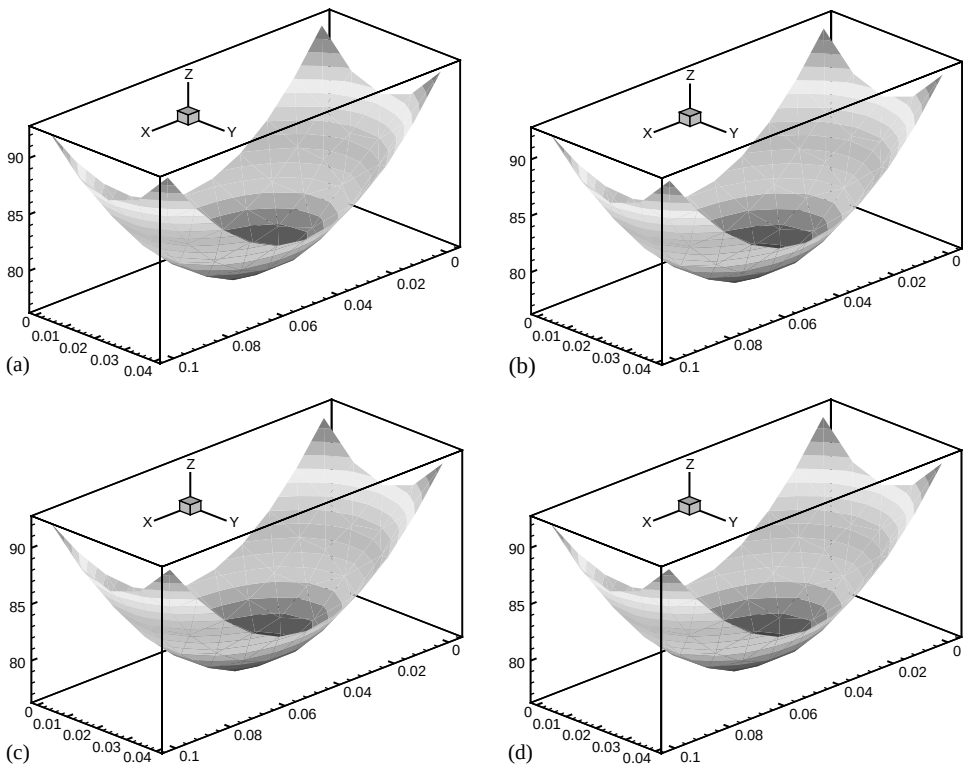

Fig. 3. Results on mesh (iii) for an isotropic case, $k_{xx} = k_{yy} = 1.2$, $h = 10$. (a) Exact solution, (b) LSPR, (c) LSF, (d) LSGR.

All tests performed using the RBF technique either caused the iterative solver to diverge or it failed to produce physically meaningful results. To understand this phenomenon it was decided to investigate the behaviour of the reconstructed functions when the exact function values were used in the RBF technique, see Figs. 7(b) and (d). These figures show the results at time, $t = 10$ s for

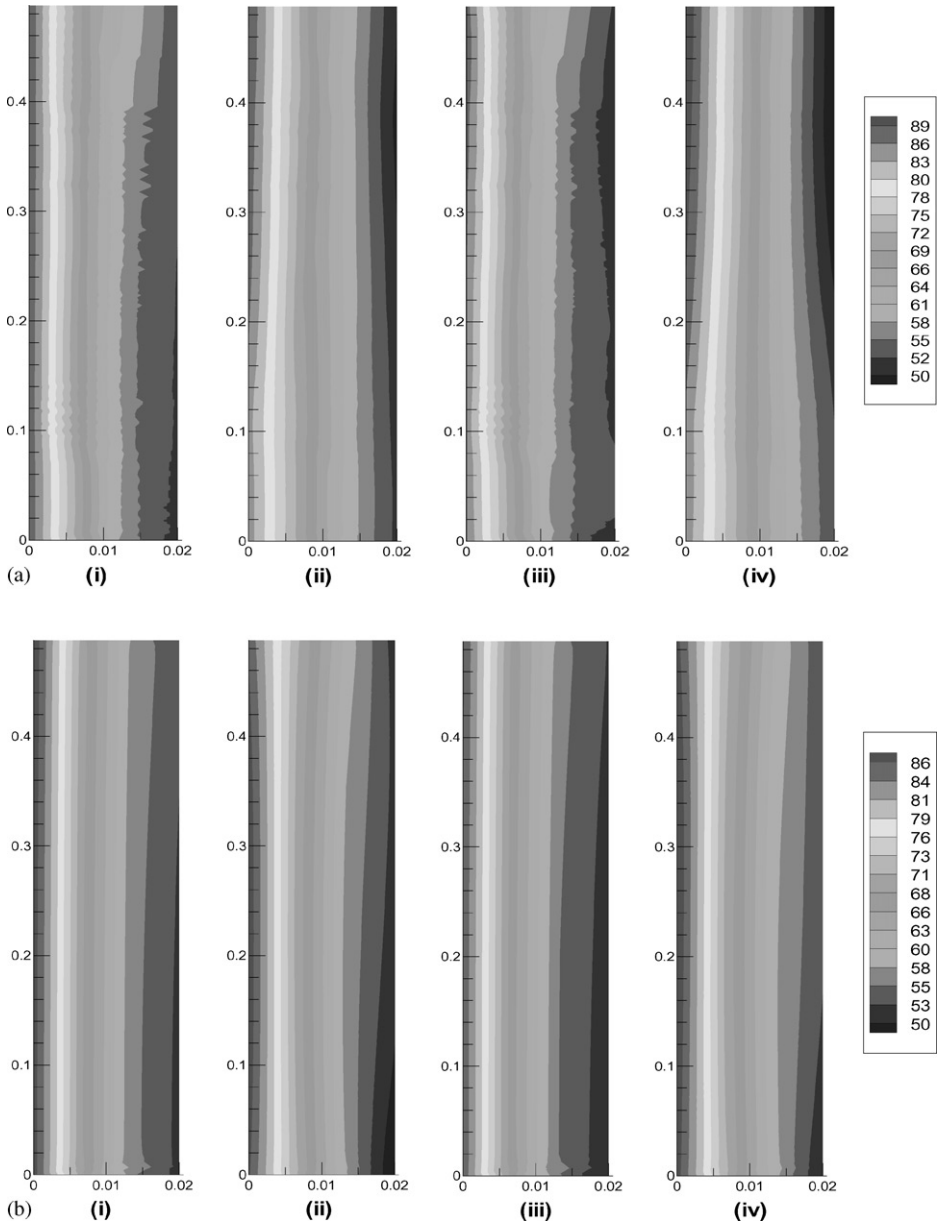

Fig. 4. Results for $k_{xx} : k_{yy} = 1 : 1000,\ h = 10$. (i) Exact solution (ii) LSF (iii) LSGR (iv) LSPR.

the cases $k_{xx} : k_{yy} = 1000 : 1$ and $k_{xx}:k_{yy} = 1 : 1000$. As can be seen from Fig. 7(d) the error observed in the reconstructed surface approximation is very significant and this error is perpetuated into the solution of the next time step, causing substantial inaccuracies in all cross-diffusion flux estimates. Fig. 7 also shows that the RBF technique, in some cases, produces an approximate function that is neither smooth nor accurate locally. This finding confirms that the RBF strategy is a reasonable

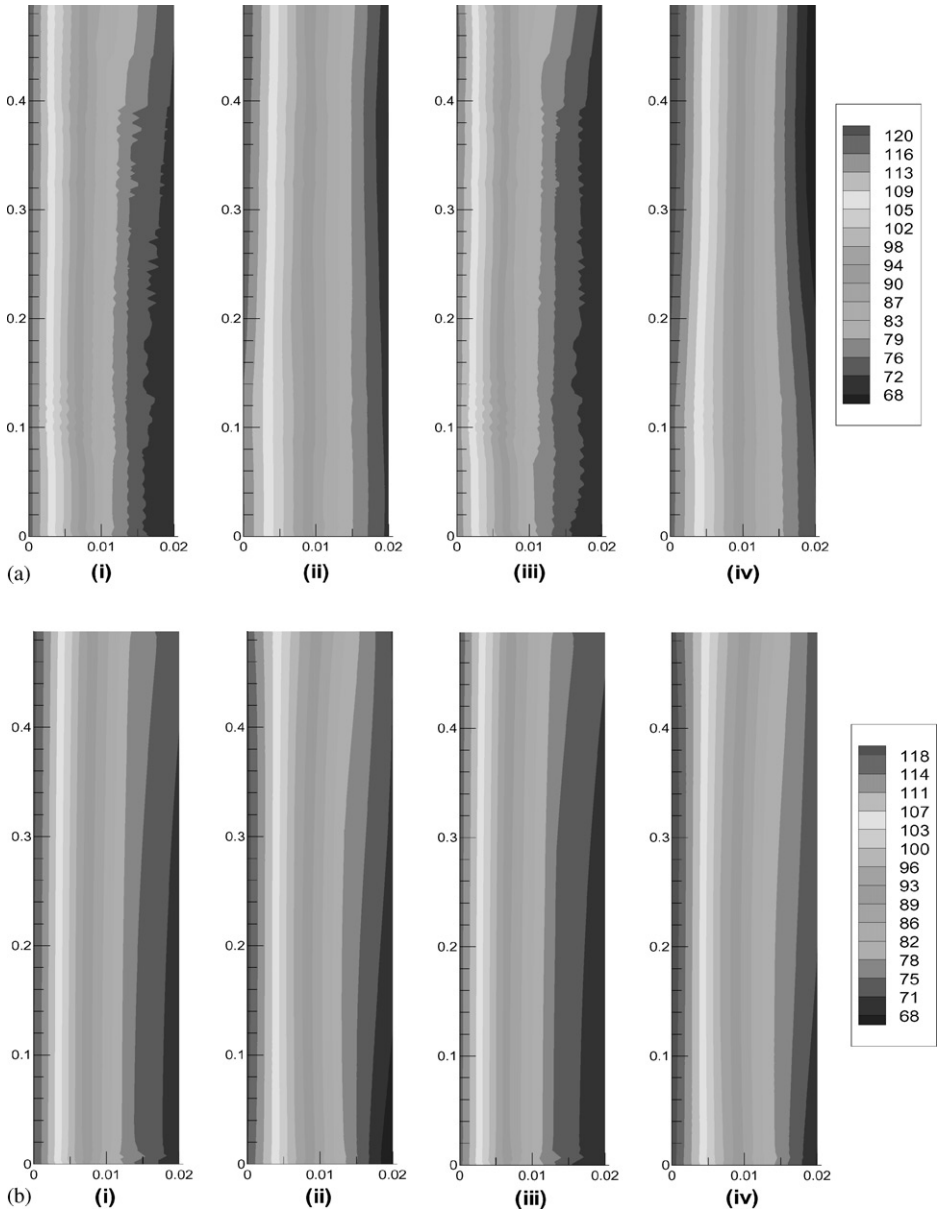

Fig. 5. Results for $k_{xx} : k_{yy} = 1 : 1000,\ h = 30$. (i) Exact solution (ii) LSF (iii) LSGR (iv) LSPR.

global interpolator but is questionable for local gradient estimation and it is therefore concluded that the RBF technique is not suitable for the construction of the secondary diffusion term for use in finite volume strategies.

The flux approximation methods presented in Sections 2.2–2.4 were tested at first on an isotropic problem and the results are shown in Fig. 3. As can be seen from this figure all methods perform

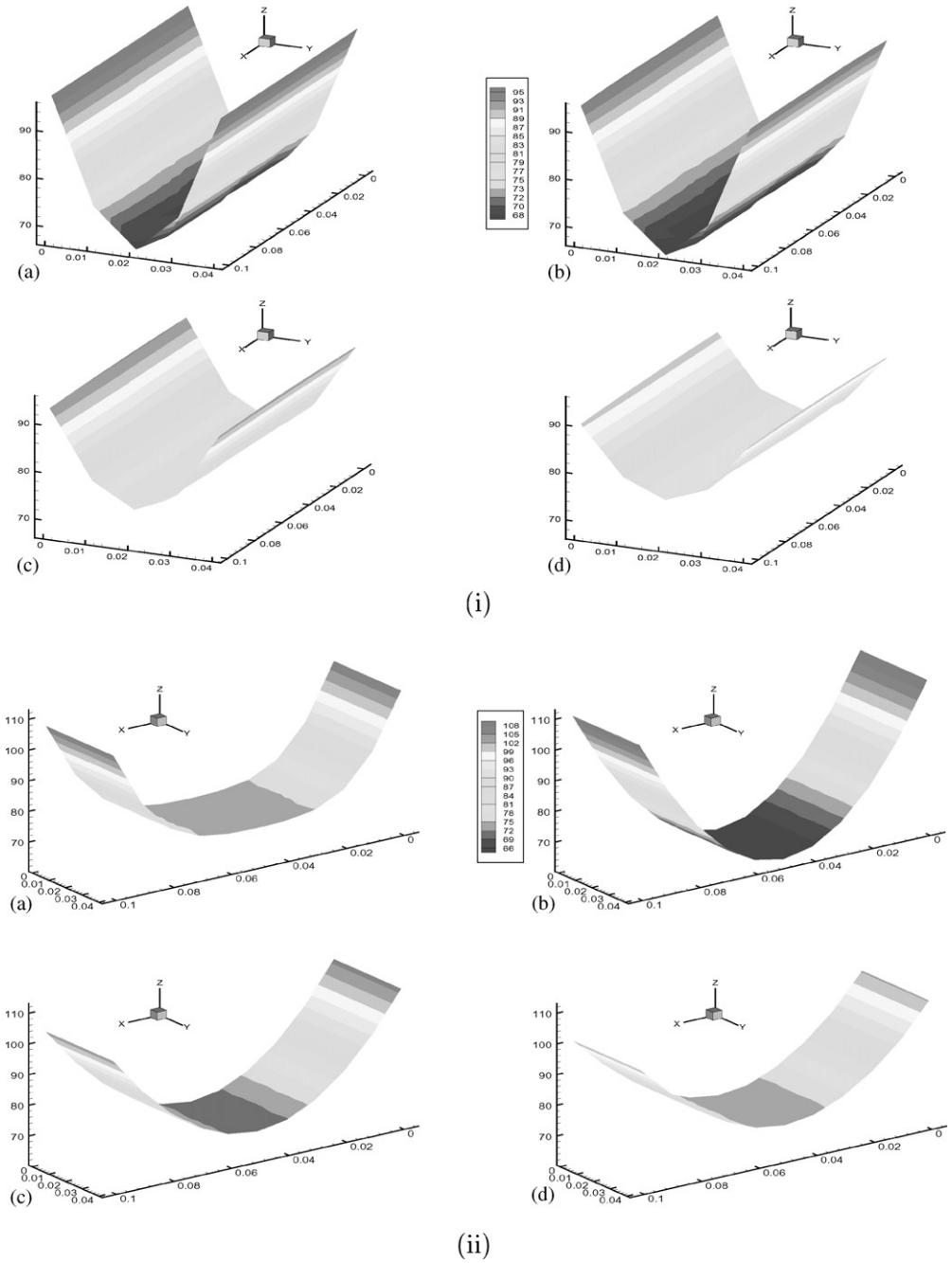

Fig. 6. Results on mesh (iii) for (i) $k_{xx} : k_{yy} = 1000 : 1$, $h = 10$. (ii) $k_{xx} : k_{yy} = 1 : 1000$, $h = 10$. (a) Exact solution (b) LSGR (c) LSPR (d) LSF.

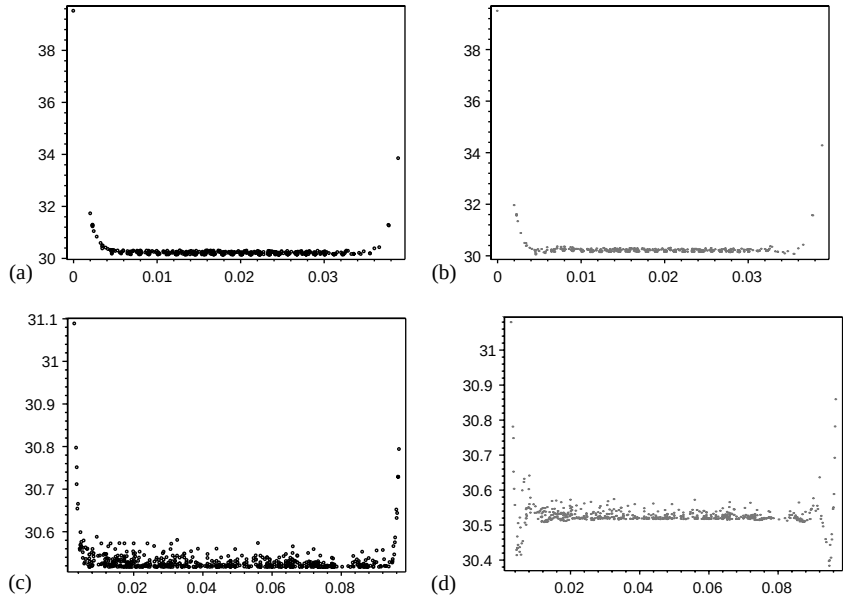

Fig. 7. A comparison of surface reconstruction using the RBF technique: (a) and (c) are exact solutions, and (b) and (d) are the approximations created using exact function values after 10 s on the domain 0.1×0.04: (a) $k_{xx} : k_{yy} = 1000 : 1$; (b) $k_{xx} : k_{yy} = 1000 : 1$; (c) $k_{xx} : k_{yy} = 1 : 1000$; (d) $k_{xx} : k_{yy} = 1 : 1000$.

well and it can be concluded that any of them can be used with confidence to model transport in isotropic media. The real test of these schemes will be discussed in the proceeding paragraphs where transport in strongly orthotropic media will be analysed.

Table 2 shows the absolute average errors (AE) between the exact and numerical solutions, computational time on a Pentium III 450 MHz PC with 256 Mb of RAM (CT) and the total number of *BiCGSTAB* iterations (TI) for cases 1–4 shown in Table 1. These results highlight the overall computational efficiency and accuracy of the least square techniques (LSGR and LSPR) for approximating the cross-diffusion term in the finite volume method when it was applied to he benchmark problem on the meshes depicted in Fig. 2. The Figs. 3–6 compare the results obtained using the techniques discussed in Sections 2.2–2.3 with the exact solution and a previously documented linear shape function method, which has been used primarily by the authors in past work for solving transport in porous media.

From Table 2, it can be seen that the least-square methods generally produce more accurate results than the linear shape function method (LSF) and well match the overall trends in the exact solution. Another observation from the table is that the number of iterations of the iterative solver *BiCGSTAB* was reduced for both of the least-square methods (LSGR and LSPR) in comparison with the shape function method. Hence, although the computational cost of the linear solver was reduced for the least-square methods, the overall CPU time was increased due to the overhead of resolving the local least-square systems for each face at every time step. In fact, for a variety of different cases studied that were not reported here due to space limitations, this was always found to be the case.

Table 2
Average error (AE), computational time (CT/s) and total number of iterations (IT) on each mesh for different h values and k_{xx}: k_{yy} ratios

	k_{xx}:k_{yy}	LSF	LSGR	LSPR	LSF	LSGR	LSPR
			Mesh (i)			Mesh (ii)	
AE							
$h = 10$	1:10	0.336149	0.501657	0.223308	0.167615	0.633174	0.237517
	1:1000	2.198415	1.138322	3.035998	1.167081	1.403330	1.335221
$h = 30$	1:10	0.824704	0.525183	0.663545	0.229429	0.682520	0.184524
	1:1000	3.808089	1.473118	5.147534	1.749353	1.785293	2.831307
CT							
$h = 10$	1:10	2.784	4.887	13.479	0.971	2.253	7.741
	1:1000	15.081	14.691	22.573	4.716	5.728	11.176
$h = 30$	1:10	2.784	4.877	13.320	0.991	2.263	7.701
	1:1000	15.302	14.541	23.133	4.766	5.608	10.966
TI							
$h = 10$	1:10	9000	8604	8000	4000	4001	4001
	1:1000	54219	44148	41799	23134	22373	21959
$h = 30$	1:10	9000	8579	8000	4002	4001	4001
	1:1000	54261	43532	46521	23255	21564	20854

In comparing the two least square methods, refer Figs. 4(a), 5(a) and 6(i), it can be seen that the LSGR method performs better than the LSPR method for the cases 2, 4 and 6. However, this is not always true, see for example Fig. 6(ii) where the anisotropy ratio is reversed (case 5) so that the dominant direction of transport is in the opposite direction. In this case LSPR technique performs better than LSGR method. For the refined mesh (ii) all methods produce good results in comparison with the exact solution, see Figs. 4(b) and 5(b). Indeed for some other cases that are not reported here, which have different geometries, boundary conditions and anisotropy ratios, the performance of all methods may still be questionable and this fact motivates the need for future research work in this field.

One explanation for the lack of performance of the LSPR method is that it uses known function values at the node points to estimate the local variation of the function in the vicinity of the face, which is then differentiated to produce the gradient. This idea could introduce additional uncertainty into the method. On the other hand, LSGR uses the function values to reconstruct the local gradients directly at the nodes, which are then averaged to give the gradient at the control volume face.

It is felt that the largest source of error arising in the flux approximation concerns the primary term, which at this point still remains first order, refer Eqs. (2) and (8). For example, since the LSGR method provides a first order approximation for the cross-diffusion term and LSPR gives a second-order approximation for this term, it must be the case that the error in the primary term dominates the flux approximation to enable the LSGR method to produce superior results to the LSPR method. Current work will seek to reduce this error by using higher order Taylor series approximations to provide a mechanism by which this dominant error can be eliminated.

4. Conclusions

In this work surface interpolation techniques have been investigated for approximating the important cross-diffusion term in the flux approximation required for use in a finite volume method. It was found that the well-known radial basis function global interpolation method is unsuitable for local gradient estimation and therefore least square methods had to be used for this purpose. In particular, the LSGR and LSPR methods performed well for the case studies presented here, providing reasonable agreement with exact solutions. Nevertheless, the research raised some issues concerning the error in the entire flux approximation, including the primary term, for a generalised finite volume methodology for treating highly anisotropic media and this finding motivates future research in this field. Work is underway considering two strategies that can be employed on any unstructured mesh in two dimensions to rectify the problems cited in the text. In the first technique a correction for the primary term of the flux will be introduced. An introduction of a correction term will be used in the second technique to increase the order of an existing fully implicit finite volume scheme to second order.

Acknowledgements

The first author wishes to acknowledge the financial support provided by the Queensland University of Technology under the IPRS scholarship program and the leave granted for the studies from the University of Ruhuna, Sri Lanka, where he is affiliated as a Lecturer.

References

[1] I. Aavatsmark, T. Barkve, Ø. Bøe, T. Mannseth, Discretization on non-orthogonal, quadrilateral grids for inhomogeneous, anisotropic media, J. Comput. Phys. 127 (1998) 2–14.
[2] C. Bailey, G.A. Taylor, M. Cross, P. Chow, Discretisation procedures for multi-physics phenomena, J. Comput. Appl. Math. 103 (1999) 3–17.
[3] T.J. Barth, Aspects of unstructured grids and finite-volume solvers for the Euler and Navier–Stokes equations, in: Lecture Notes Presented at the VKI Lecture Series 1994-05, February.
[4] P. Chow, M. Cross, K. Pericleous, A natural extension of the conventional finite volume method into polygonal unstructured meshes for CFD application, Appl. Math. Modelling 20 (1996) 170–183.
[5] L. Davidson, L. Stolcis, An efficient and stable solution procedure of turbulent flow on general unstructured meshes using transport turbulence models, in: AIAA—33rd Aerospace Sciences Meeting and Exhibit, Reno, NV, US, AIAA-95-0342, 1995.
[6] I. Demirdžić, S. Muzaferija, Numerical method for coupled fluid flow, heat transfer and stress analysis using unstructured moving meshes with cells of arbitrary topology, Comput. Methods Appl. Mech. Eng. 125 (1995) 235–255.
[7] W.J. Ferguson, The control volume finite element numerical solution technique applied to creep in softwoods, Internat. J. Solids Structures 35 (13) (1998) 1325–1338.
[8] P.A. Forsyth, A control volume finite element approach to NAPL groundwater contamination, SIAM J. Sci. Statist. Comput. 12 (5) (1991) 1029–1057.
[9] C. Helf, U. Küster, A finite volume method with arbitrary polygonal control volumes and high order reconstruction for the Euler equations, CFD Conference Proceedings, European Community on Computational methods in Applied Sciences, Wiley, New York, 1994.

[10] C. Ilinca, X.D. Zhang, J.-Y. Trépanier, R. Camarero, A comparison of three error estimation techniques for finite-volume solutions of compressible flows, Comput. Methods Appl. Mech. Eng. 189 (2000) 1277–1294.
[11] P.A. Jayantha, I.W. Turner, A comparison of gradient approximations for use in finite-volume computational models for two-dimensional diffusion equations, Numer. Heat Transfer, Part B: Fundam. 40 (5) (2001) 367–390.
[12] P.A. Jayantha, I.W. Turner, Generalised finite volume strategies for simulating transport in strongly orthotropic porous media, in: Proceedings of the 10th Biennial Computational Techniques and Applications Conference—CTAC2001, Australian and New Zealand Industrial and Applied Mathematics Journal, to appear.
[13] E.J. Kansa, Multiquadratics—A scattered data approximation scheme with applications to computational fluid dynamics-I, Comput. Math. Appl. 19 (8/9) (1990) 127–145.
[14] N.O. Moraga, E.E. Medina, Conjugate forced convection and heat conduction with freezing of water content in a plate shaped food, Internat. J. Heat Mass Transfer 43 (2000) 53–67.
[15] J.Y. Murthy, S.R. Mathur, Computation of anisotropic conduction using unstructured meshes, J. Heat Transfer 120 (1998) 583–591.
[16] B. Niceno, "EasyMesh" (Version 1.4), freely available mesh generator on the web site: http://www-dinma.univ.trieste.it/~nirftc/research/easymesh/.
[17] P.J. Oliveira, On the numerical implementation of nonlinear viscoelastic models in a finite-volume method, Numer. Heat Transfer, Part B: Fundam. 40 (2001) 283–301.
[18] S.V. Patankar, Numerical Heat Transfer and Fluid Flow, Hemisphere Publishing Corporation, Washington, DC, 1980.
[19] P. Perré, I. Turner, TransPore: a generic heat and mass transfer computational model for understanding and visualising the drying of porous media (Invited paper), Drying Technol. J. 17 (7) (1999) 1273–1289.
[20] K. Riemslagh, J. Vierendeels, E. Dick, An arbitrary Lagrangian–Eulerian finite volume method for the simulation of rotary displacement pump flow, Appl. Numer. Math. 32 (2000) 419–433.
[21] E. Turkel, Accuracy of schemes with nonuniform meshes for compressible fluid flows, Institute for Computer Applications in Science and Engineering, Report No. 85-43, National Aeronautics Space Administration, Virginia, 1985.
[22] I.W. Turner, W.J. Ferguson, An unstructured mesh cell-centered control volume method for simulating heat and mass transfer in porous media: application to softwood drying-Part I: the anisotropic model, Appl. Math. Modelling 19 (1995) 668–674.
[23] H.V. van der Vorst, BI-CGSTAB: a fast and smoothly converging variant of BI-CG for the solutions of nonsymmetric linear system, SIAM J. Sci. Statist. Comput. 13 (2) (1992) 631–644.
[24] P. Vijayan, Y. Kallinders, A 3D finite-volume scheme for the Euler equations on adaptive tetrahedral grids, J. Comput. Phys. 133 (1994) 249–267.
[25] A.S.M. Wong, Y.C. Hong, T.S. Li, S.L. Chung, E.J. Kansa, Multizone decomposition for simulation of time-dependent problems using the multiquadratic scheme, Internat. J. Comput. Math. Appl. 37 (1999) 23–43.
[26] S.-C. Xue, R.I. Tanner, N. Phan-Thien, Three-dimensional numerical simulations of viscoelastic flows—Predictability and accuracy, Comput. Methods Appl. Mech. Eng. 180 (1999) 305–331.